HAL
open science

Frequency spectrum of the geomagnetic field harmonic coefficients from dynamo simulations

Claire Bouligand, Nicolas Gillet, Dominique Jault, Nathanaël Schaeffer, Alexandre Fournier, Julien Aubert

To cite this version:

Claire Bouligand, Nicolas Gillet, Dominique Jault, Nathanaël Schaeffer, Alexandre Fournier, et al.. Frequency spectrum of the geomagnetic field harmonic coefficients from dynamo simulations. Geophysical Journal International, 2016, 207, pp.1142 - 1157. 10.1093/gji/ggw326 . hal-01451189

HAL Id: hal-01451189

https://hal.science/hal-01451189

Submitted on 31 Jan 2017

HAL is a multi-disciplinary open access archive for the deposit and dissemination of scientific research documents, whether they are published or not. The documents may come from teaching and research institutions in France or abroad, or from public or private research centers.

L'archive ouverte pluridisciplinaire **HAL**, est destinée au dépôt et à la diffusion de documents scientifiques de niveau recherche, publiés ou non, émanant des établissements d'enseignement et de recherche français ou étrangers, des laboratoires publics ou privés.

submitted to *Geophys. J. Int.*

Frequency spectrum of the geomagnetic field harmonic coefficients from dynamo simulations

C. Bouligand[1], N. Gillet[1], D. Jault[1], N. Schaeffer[1], A. Fournier[2], J. Aubert[2]

[1] *Univ. Grenoble Alpes, CNRS, ISTerre, F-38000 Grenoble, France.*

[2] *Institut de Physique du Globe de Paris, Sorbonne Paris Cité, Univ. Paris Diderot, CNRS, 1 rue Jussieu, F-75005 Paris, France.*

SUMMARY

The construction of geomagnetic, archeomagnetic or paleomagnetic field models requires some prior knowledge about the actual field, which can be gathered from the statistical properties of the field over a variety of length-scales and time-scales. However, available geomagnetic data on centennial to millennial periods are too sparse to infer directly these statistical properties. We thus use high-resolution numerical simulations of the geodynamo to test a method for estimating the temporal power spectra (or equivalently the auto-covariance functions) of the individual Gauss coefficients that describe the geomagnetic field outside the Earth's fluid outer core. Based on the spectral analysis of our simulations, we argue that a prior for the observational geomagnetic field over decennial to millennial periods can be constructed from the statistics of the field during the short satellite era. The method rests on the assumption that time series of spherical harmonic coefficients can be considered as realisations of stationary and differentiable stochastic processes, namely order 2 autoregressive (AR2) processes. In the framework of these processes, the statistics of Gauss coefficients are well constrained by their variance and one or two time-scales. We find that the time spectra in the dynamo simulations of all Gauss coefficients but the axial dipole are well approximated by the spectra of AR2 processes characterized by only

one timescale. The process parameters can simply be deduced from instantaneous estimates of the spatial power spectra of the magnetic field and of its first time derivative. Some deviations of the Gauss coefficients statistics from this minimal model are also discussed. Characterizing the axial dipole clearly requires a more sophisticated AR2 process, with a second distinct time-scale.

Key words: Dynamo: theories and simulations; Magnetic field; Rapid time variations; Probability distributions; Time-series analysis; Inverse theory.

1 INTRODUCTION

The construction of global field models or of regional master-curves from geomagnetic records has required the use of spatial and temporal regularizations (e.g., Jackson et al. 2000; Korte et al. 2009; Thébault and Gallet 2010). Searching for models as smooth as possible (e.g., Constable and Parker 1988a) allows to retrieve the features that are reliably constrained by the data, but does not give access to uncertainties on model coefficients. To address this issue, geomagnetic models have been produced using prior information in the form of covariance matrices for the model parameters. These matrices have been built using either some knowledge of the temporal variability of the present geomagnetic field, which we will further discuss here, or spatial cross-covariances deduced from geodynamo simulations (e.g., Fournier et al. 2013, 2015). Such prior information is particularly useful when modeling the Earth's magnetic field on historical and archeological time-scales, for which the data distribution is sparse in both space and time, and is characterized by large measurements (and sometimes dating) errors. Finally, prior information in the form of covariance matrices is a prerequisite for data assimilation. For instance, knowledge of the analysis covariance matrix in sequential assimilation is necessary to forecast future trajectories of the geomagnetic field (e.g., Gillet et al. 2015; Aubert 2015).

In the probabilistic framework of assimilation algorithms, geomagnetic spherical harmonic coefficients are assumed to result from Gaussian processes. These are stationary stochastic processes fully specified by their means and auto-covariance functions (MacKay 1998). As a matter of fact, the auto-covariance function of any stationary stochastic process can be deduced from its frequency spectrum. Analyses of geomagnetic records suggest that their power spectrum P behaves as $P(f) \propto f^{-s}$ in some ranges of frequency f, with s the spectral index (e.g., Constable and Johnson 2005; Panovska et al. 2013). This defines scale invariance. The index value is related to the underlying physical processes and to the statistical properties of the time-series.

Studies of the Earth dipole moment (Constable and Johnson 2005) suggest a flat energy density

spectrum ($s = 0$) for the longest time-scales (1 Myr or more). This spectrum steepens towards higher frequencies, with a spectral index $s \simeq 2$ at millennial to centennial time-scales (Panovska et al. 2013) and $s \simeq 4$ from centennial to inter-annual time-scales (De Santis et al. 2003). Considering the unsigned dipole moment for the past 2 Myr, Brendel et al. (2007) and Buffett et al. (2013) found that its spectrum, over millennial periods, has also a spectral index of 2, and made the analogy with spectra from realisations of autoregressive stochastic processes of order one (AR1). These processes have continuous but non differentiable samples. They are also known as Ornstein-Uhlenbeck processes and are solutions of a Langevin-type equation (Gardiner 1985). Buffett et al. (2013) argued that the characteristic time-scale of the deterministic part of the stochastic process that they constructed from dipole series is set by the dipole decay time t_d. In this framework, this time is related to the escape time for bistable systems that they also connect to the rate of magnetic reversals. Buffett (2015) also studied the relation of this time to the duration of polarity transitions.

Although the axial dipole field has been the focus of many studies, the non-dipolar field is much less documented. On time-scales shorter than a few centuries, order 2 autoregressive (AR2) stochastic processes, whose samples are differentiable, have been introduced to define prior information about the auto-covariance function of the Gauss coefficients when building global magnetic field models over the observatory era (Gillet et al. 2013) and regional models over archeological periods (Hellio et al. 2014). They are indeed consistent with a spectral index $s = 4$ at decadal periods. Gillet et al. (2013) characterized the appropriate AR2 stochastic process from the variance and the secular variation times of the spherical harmonic coefficients. They calculated these two quantities from the geomagnetic spatial power spectrum of the geomagnetic field (Lowes 1974) and of its time-derivative (the secular variation) obtained from a field model of the well documented satellite era. Considering geomagnetic series as sample functions of stochastic processes with power spectrum $P(f) \propto f^{-4}$ gives an explanation to the occurrence of geomagnetic jerks, which are defined as abrupt changes in the geomagnetic field second time derivative (Mandea et al. 2010).

Constructing field models from realisations of AR2 processes yields time series very similar to observatory series (Brown 2015). However, the hypothesis that Gauss coefficients can be described in terms of AR2 stochastic processes is not easily tested using geomagnetic observations because we lack highly accurate, dense coverage data over a long enough time window. In particular, the satellite era is too short in comparison with the decadal to centennial correlation times involved in the evolution of the geomagnetic field. For this reason, it may be helpful to investigate the statistics of individual coefficient series from numerical simulations of the geodynamo. Although calculated for dimensionless numbers far from Earth-like parameters, numerical simulations provide us with time series of Gauss coefficients that may be used to test assumptions about the statistics of the field

coefficients (Kuipers et al. 2009; Tanriverdi and Tilgner 2011; Meduri and Wicht 2016). A major issue is the rescaling of the time axis (Lhuillier et al. 2011b; Christensen et al. 2012). Buffett et al. (2014) and Buffett and Matsui (2015) have just achieved a comparison between the frequency spectrum of the dipole term obtained from a numerical simulation and the theoretical spectrum expected for a stochastic process. In both numerical and theoretical spectra, they distinguished three domains of increasing frequencies for which the spectral index is, as described above for the observed field, $s = 0$, $s = 2$ and $s = 4$. Then, they documented the transitions between the three frequency ranges, and proposed a phenomenological interpretation of the two cut-off times: they suggest that they are related to the dipole decay time t_d and to the lifetime of convective eddies in the fluid core. Attributing the different times to specific underlying mechanisms in the geodynamo models may help to compare simulations and observations and to overcome the limitations of the numerical models.

Instead of focusing our analysis on the dipole field, we apply here stochastic modeling to spherical harmonics of higher degree. We use high-resolution numerical simulations to test a simple recipe for the auto-covariance function of the geomagnetic coefficients based on instantaneous models of the field and its time variation. We find that the AR2 stochastic processes recently used as prior by Gillet et al. (2013) and Hellio et al. (2014) do provide an approximation of the temporal power spectra for individual Gauss coefficients in the numerical simulations. Based on these results, we argue that up to millennial periods the auto-covariance function of Gauss coefficients of the actual geomagnetic field can be described with only two parameters (or three for the axial dipole).

The manuscript is organized as follows. In section 2, we give an overview of stochastic processes that we consider in this study to model the time evolution of geomagnetic Gauss coefficients. In section 3, we first give the main characteristics of the three different numerical dynamo simulations analysed throughout this study, before we describe the statistics (variance, correlation time and spectra) of the generated Gauss coefficients. Next, we compare the frequency spectra of non-dipole Gauss coefficients in our dynamo simulations with spectra predicted from the assumption that they are realisations of order 2 stochastic processes with a single characteristic time-scale. Finally in section 4 we describe possible deviations from spherical symmetry, and discuss the specific behavior of the axial dipole at millennial and longer periods. Those considerations lead us to speculate about the possible mechanisms underlying the time-scales of the stochastic processes that we have considered. We finally discuss consequences for uncertainty estimates in field modeling.

2 STOCHASTIC MODELS FOR THE TIME EVOLUTION OF GAUSS COEFFICIENTS

As stated by the Wiener-Khinchin theorem (Van Kampen 2007), a stationary stochastic process x of time t can be characterized either by its power spectrum $P(f)$ or by its auto-covariance function

$C(\tau) = E(x(t)x(t+\tau))$, where $E(\ldots)$ stands for the statistical expectation. Those two quantities are related through

$$P(f) = \int_{-\infty}^{\infty} C(\tau) e^{-i2\pi f\tau} \mathrm{d}\tau \,. \tag{1}$$

We make below a connection between the stochastic processes that we use in this study and the processes that have been previously employed to model the evolution of the geocentric axial dipole.

2.1 A three-parameter AR2 process for the axial dipole

Transition between power laws $P(f) \propto f^{-4}$, f^{-2}, and f^0 at respectively high, intermediate and low frequencies have been documented for the Earth magnetic field (e.g., Constable and Johnson 2005; Ziegler et al. 2011) as well as for dynamo numerical simulations (Olson et al. 2012; Davies and Constable 2014; Buffett and Matsui 2015). Based on these observations, Hellio (2015) and Buffett and Matsui (2015) introduced specific stochastic processes for modeling the time changes of the axial dipole. Their two approaches are compared below.

In the following, we assume that the axial dipole coefficient samples a stochastic process $x(t)$, of non-zero average $\bar{x} = E(x)$, i.e. we consider a period of constant (normal or inverse) polarity. We discuss the fluctuations $y(t) = x(t) - \bar{x}$ about this average. Hellio et al. (2014) proposed that y is a realisation of an AR2 stochastic process, namely is solution of a differential equation of the form

$$\frac{\mathrm{d}^2 y}{\mathrm{d}t^2} + 2\chi \frac{\mathrm{d}y}{\mathrm{d}t} + \omega^2 y = \zeta(t) \,, \tag{2}$$

where $\zeta(t)$ is a white noise process, and the frequencies ω and χ are positive. The latter two conditions ensure that the process is stationary. For $\chi > \omega$, the frequency spectrum exhibits f^{-4}, f^{-2} and f^0 dependence at respectively high, intermediate and low frequencies. It can be expressed as (e.g. Yaglom 2004)

$$P(f) = \frac{4\chi\omega^2\sigma^2}{\left(\omega^2 - (2\pi f)^2\right)^2 + (4\pi\chi f)^2} \,, \tag{3}$$

where $\sigma^2 = E\left(y^2\right)$. It is thus constrained by three quantities: the process variance σ^2, and the parameters χ and ω. The auto-covariance function is given by

$$C(\tau) = \frac{\sigma^2}{2\xi} \left((\chi + \xi) e^{-(\chi-\xi)|\tau|} - (\chi - \xi) e^{-(\chi+\xi)|\tau|} \right) \,, \tag{4}$$

with $\xi^2 = \chi^2 - \omega^2$. The time ω^{-1} can be obtained as the square root of the ratio between the variance of y and of its time derivative (Hellio 2015, p.50). Indeed, the auto-covariance function C is twice differentiable at $\tau = 0$, with

$$C''(0) = \left.\frac{\mathrm{d}^2}{\mathrm{d}\tau^2} C(\tau)\right|_{\tau=0} = -\sigma^2\omega^2 \,, \tag{5}$$

and we have also (Hulot and Le Mouël 1994):

$$C''(0) = -E\left[\left(\frac{\mathrm{d}y}{dt}(t)\right)^2\right] . \tag{6}$$

Buffett and Matsui (2015) model instead the evolution of $x(t)$ using the stochastic equation

$$\frac{\mathrm{d}x}{\mathrm{d}t} = v(x) + \sqrt{D(x)}\Gamma(t)\,, \tag{7}$$

where $\Gamma(t)$ is a red noise characterized by a Laplacian auto-covariance function, $v(x)$ is a drift term describing the slow evolution of the axial dipole moment, and $D(x)$ defines the amplitude of random fluctuations. Following Buffett et al. (2013, 2014) and Buffett and Matsui (2015), the latter two terms may be approximated by $v(x) \simeq -(x-\bar{x})/\tau_s = -y/\tau_s$ and $D(x) \simeq D$, yielding a stochastic equation of the form

$$\frac{\mathrm{d}y}{\mathrm{d}t} + \frac{y}{\tau_s} = \epsilon(t)\,, \tag{8}$$

with $\epsilon(t) = \sqrt{D}\Gamma(t)$. Since $\epsilon(t)$ is a Laplacian correlated noise, its evolution can be modeled by an order one stochastic equation of the form (e.g., Jazwinski 2007)

$$\frac{\mathrm{d}\epsilon}{\mathrm{d}t} + \frac{\epsilon}{\tau_f} = \zeta(t)\,, \tag{9}$$

with $\zeta(t)$ a white noise process.

Combining equations (8) and (9) leads to an equation of the form

$$\frac{\mathrm{d}^2y}{\mathrm{d}t^2} + \left(\frac{1}{\tau_s} + \frac{1}{\tau_f}\right)\frac{\mathrm{d}y}{\mathrm{d}t} + \frac{y}{\tau_s\tau_f} = \zeta(t)\,. \tag{10}$$

With $2\chi = 1/\tau_s + 1/\tau_f$ and $\omega^2 = 1/(\tau_s\tau_f)$, equation (10) defines an AR2 stochastic process similar to that defined through equation (2). Adopting $\tau_f < \tau_s$, we obtain

$$\begin{cases} \tau_s = & \dfrac{\chi+\xi}{\omega^2} \\ \tau_f = & \dfrac{\chi-\xi}{\omega^2} \end{cases} . \tag{11}$$

For $\tau_f \ll \tau_s$, we deduce from (3) and (11) that the transition period between domains of the power spectrum presenting 2 and 4 (resp. 0 and 2) spectral indices is $2\pi\tau_f$ (resp. $2\pi\tau_s$).

Hellio (2015) and Buffett et al. (2013) are therefore using similar stochastic models for the axial dipole. Note however that the latter implicitly states the condition ξ real and $\chi \geq \omega$ – see equation (11). Equation (2) is thus more general, and allows a wider range of behaviors.

2.2 A two-parameter AR2 process for non dipole coefficients

For an AR2 process with $\chi = \omega$ (*i. e.* $\tau_f = \tau_s$), the frequency spectrum of the process defined from (2) is given by

$$P(f) = \frac{4\omega^3\sigma^2}{\left[\omega^2 + (2\pi f)^2\right]^2} \,. \tag{12}$$

This power spectrum is flat (spectral index $s = 0$) at low frequencies and behaves as f^{-4} for $f \gg \omega/(2\pi)$. It does not display a power law f^{-2} at intermediate frequencies. The auto-covariance function of the process is given by

$$C(\tau) = \sigma^2 \left(1 + \omega|\tau|\right) e^{-\omega|\tau|} \,. \tag{13}$$

This particular autoregressive process of order 2 depends only on two parameters, the variance σ^2 and the characteristic time-scale ω^{-1}. It was used by Gillet et al. (2013), Hellio et al. (2014), and Hellio (2015) to define prior information on Gauss coefficients for the computation of global archeomagnetic and geomagnetic field models.

3 METHOD FOR CHARACTERIZING THE TIME-SPECTRA OF GAUSS COEFFICIENTS

Assuming that all Gauss coefficients but the axial dipole sample stochastic Gaussian processes of auto-covariance function (13), we use numerical geodynamo simulations to discuss how to estimate the two parameters σ and ω that characterize the processes. Then, we compare the theoretical power spectrum of these processes to the actual spectrum of the Gauss coefficients in our numerical simulations.

3.1 Simulations used in the study

We rely on three dynamo numerical simulations named Step 0 (S0), Step 1 (S1), and Coupled Earth (CE). All three solve the momentum, codensity and induction equations under the Boussinesq approximation, for an electrically conducting fluid within a spherical shell of aspect ratio 0.35 between the inner core and the outer core of radius c. S0 and S1 were computed using the free XSHELLS code (Schaeffer 2015), assuming no-slip and fixed homogeneous heat flux conditions at both the inner and outer boundaries. CE (Aubert et al. 2013) was run using the PARODY-JA code (Aubert et al. 2008), assuming no-slip conditions at the inner boundary, free-slip conditions at the outer core boundary, and heterogeneous mass-anomaly flux both at the inner and at the outer boundaries. This simulation also includes a gravitational coupling between the inner core and the mantle. Both codes use finite differences in radius and spherical harmonic expansion (Schaeffer 2013), together with a semi-implicit Crank-Nicolson-Adams-Bashforth time scheme of order 2.

Non-dimensional parameters and times characterizing these simulations are given in Table 1. Dimensionless times are transformed into years following Lhuillier et al. (2011b) – see also sections 3.2 and 4.3. The field intensity is also rescaled to dimensional units using a proportionality constant such

that the averaged root mean square (r.m.s.) field in the shell is equal to 4 mT, a value comparable to that estimated for the Earth's core by Gillet et al. (2010).

The longest simulations S0 and CE allow to investigate long time-scales, whereas the high sampling rate and the small Ekman number in S1 give access to shorter time-scales. All three simulations are dipole-dominated at the Core Mantle Boundary (CMB); see the relative dipole field strength f_{dip} in Table 1. They also display non-dipolar structures and significant secular variation (but no polarity reversal). The field in CE has the particularity to show prominent equatorial structures that undergo a westward drift, as observed for the Earth's magnetic field over the past four centuries (Finlay and Jackson 2003). It is also important to notice that the magnetic Reynolds number Rm (defined as the ratio of magnetic diffusion time over advection time) in our three simulations is close to the Earth's core value (see Table 1).

Statistics over periods much longer than a few 10,000 years (e.g. involving reversals) would require much longer simulations. There is thus a trade-off between capturing the long term evolution of dipole moment changes and reproducing rapid field variations (Meduri and Wicht 2016). Robust estimates of the mean dipole field strength require simulations over many diffusion times that are presently achievable only for large Ekman number (e.g., Olson et al. 2012; Davies and Constable 2014). Because we are particularly interested here into decadal to millennial time-scales, we use parameters closer to (yet still far away from) the geophysical ones. Our simulations thus cover a wide range of periods shorter than the turn-over time t_U.

We show in Fig. 1 and 2 examples of the time series that we analyse in the rest of the paper. The axial dipole has a non-zero mean value and displays large long-period fluctuations. We observe a decrease of both the amplitude and the time-scale of fluctuations of the other coefficients with degree. While temporal fluctuations of all coefficients seem rather stationary in simulations S0 and CE (Fig. 1), non-stationarity is observed in the shorter simulation S1 for the largest degrees (Fig. 2, right). Note that periodic oscillations are observed for coefficient $\mathcal{G}_2^1$ in CE. These oscillations will be discussed in section 4.2.

3.2 Variance and correlation time of Gauss coefficients

The magnetic field $\mathbf{B}$ outside the core is described through a scalar potential V such that $\mathbf{B} = -\nabla V$. In this work, Gauss coefficients $\mathcal{G}_n^m$ and $\mathcal{H}_n^m$ are defined at the core surface (and not at the Earth's surface) with n and m the spherical harmonics degree and order, N the truncation degree, hence V is decomposed as

$$V(r,\theta,\phi,t) = c\sum_{n=1}^{N}\left(\frac{c}{r}\right)^{n+1}\sum_{m=0}^{n}\left(\mathcal{G}_n^m(t)\cos m\phi + \mathcal{H}_n^m(t)\sin m\phi\right)P_n^m(\cos\theta)\,, \tag{14}$$

Name	Definition	S0	S1	CE	C-600	C-1400	Earth's core
Ekman	$E = \nu/(\Omega D^2)$	10^{-5}	10^{-6}	$3\,10^{-5}$	$5\,10^{-5}$	$5\,10^{-5}$	$4\,10^{-15}$
Flux Rayleigh	$Ra_F = FD^2/4\pi\rho\kappa^2\nu$	$4.4\,10^{10}$	$8.9\,10^{11}$	$1.0\,10^{9}$	$3.1\,10^{7}$	$1.5\,10^{8}$	?
Magnetic Reynolds	$Rm = UD/\eta$	710	660	940	42	90	1700
Prandtl	$Pr = \nu/\kappa$	1	1	1	1	1	$0.1 - 10$
Magnetic Prandtl	$Pm = \nu/\eta$	0.4	0.2	2.5	0.5	0.5	$2\,10^{-6}$
Alfvén time	$t_A = D\sqrt{\mu_0\rho}/B$	100	47	110		83	2
Dipole decay time	$t_d = c^2/(\pi^2\eta)$	$1.2\,10^4$	$1.2\,10^4$	$3.2\,10^4$	$1.2\,10^3$	$2.7\,10^3$	$5\,10^4$
Turn-over time	$t_U = D/U$	69	76	140	120	120	120
Dissipation time†	τ_{diss}^{mag}	12	14.5	41			
Dipole field strength‡	f_{dip}	0.73	0.68	0.75			0.68
Simulation duration		$85.\,10^3$	$7.6\,10^3$	$84.\,10^3$		$91.\,10^3$	
Sampling interval		38	0.25	5.3		11	

Table 1. Non-dimensional numbers and time-scales for numerical simulations and the Earth's core. All times are given in years. D is the shell thickness, c is the outer core radius, B and U the root mean square of the magnetic field intensity and of the velocity in the fluid shell, Ω the rotation rate, η the magnetic diffusivity, ν the kinematic viscosity, κ the thermal diffusivity, μ_0 the magnetic permeability of free space, F the mass anomaly flux at the Inner-Core boundary (chemical convection, see Aubert et al. 2013). C-600 and C-1400 stand for the Calypso simulations of Buffett and Matsui (2015), after translating their time-scale into the τ_{SV}-based scaling used throughout this paper, with $\tau_{SV} = 14\,t_d/Rm$ (Lhuillier et al. 2011a). See Backus et al. (1996, pp 200-204) for the calculation of the dipole decay time t_d. †We refer to Christensen and Tilgner (2004) for the definition of the magnetic dissipation time τ_{diss}^{mag}, ratio of magnetic energy to Ohmic dissipation. ‡The relative dipole field strength at the core surface f_{dip} is defined as in Christensen and Aubert (2006). We have adopted $\nu = 1.5\,10^{-6}\,\mathrm{m^2s^{-1}}$, $\eta = 0.75\,\mathrm{m^2s^{-1}}$, $\rho = 1.1\,10^4\,\mathrm{kg.m^{-3}}$, $\tau_{SV} = 415\,\mathrm{yrs}$ and $B = 4\,10^{-3}\,\mathrm{T}$ to give values for the Earth's core. The turn-over time deduced from τ_{SV} and Lhuillier et al. (2011a), $t_U = D/U \simeq 0.3\,\tau_{SV} \simeq 125\,\mathrm{yrs}$, is consistent with $U \sim 20\,\mathrm{km.yr^{-1}}$ in the Earth's core and is within a factor of two of our estimates from simulations.

where r is the distance to the Earth center, θ the colatitude, ϕ the longitude, and P_n^m are the Schmidt quasi-normalized Legendre functions. We define the spatial power spectra for the geomagnetic field and its secular variation

$$\left\{\begin{array}{ll} R_n = & (n+1)\displaystyle\sum_{m=0}^{n}\Big[E(\mathcal{G}_n^{m2}) + E(\mathcal{H}_n^{m2})\Big] \\ S_n = & (n+1)\displaystyle\sum_{m=0}^{n}\Big[E(\partial_t\mathcal{G}_n^{m2}) + E(\partial_t\mathcal{H}_n^{m2})\Big] \end{array}\right. \tag{15}$$

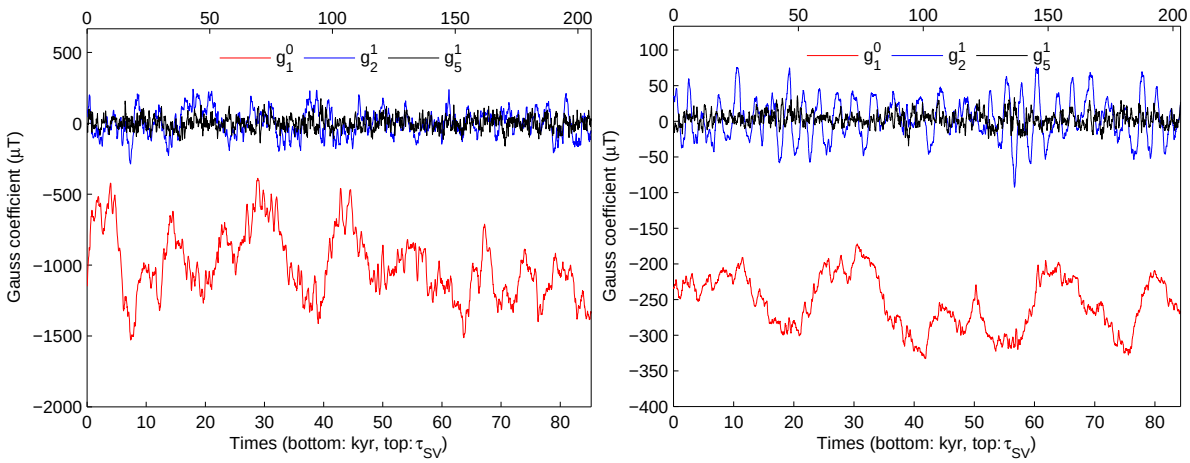

Figure 1. Time series of coefficients $\mathcal{G}_1^0$, $\mathcal{G}_2^1$ and $\mathcal{G}_5^1$ from simulations S0 (left) and CE (right). The top scale gives the dimensionless time (based on τ_{SV}).

as functions of degree n, from which a correlation time $\tau_n = \sqrt{R_n/S_n}$ can be derived (Hulot and Le Mouël 1994).

The two quantities R_n and τ_n are now assumed to follow simple laws as a function of the degree n (for $n \geq 2$):

$$R_n \simeq \alpha\beta^n, \qquad \tau_n \simeq \delta n^{-\gamma} \ . \tag{16}$$

Constable and Parker (1988b) found that geomagnetic field models ($1 \leq n \leq 12$) are consistent with $\beta = 1$, whereas Roberts et al. (2003) inferred $\beta \simeq 0.90$ from observations for $n \geq 3$. Holme and Olsen (2006) and Lesur et al. (2008) examined their satellite field models and estimated $\gamma \simeq 1.45$ and $\gamma \simeq 1.375$ respectively whereas Christensen and Tilgner (2004) and Lhuillier et al. (2011b) argued

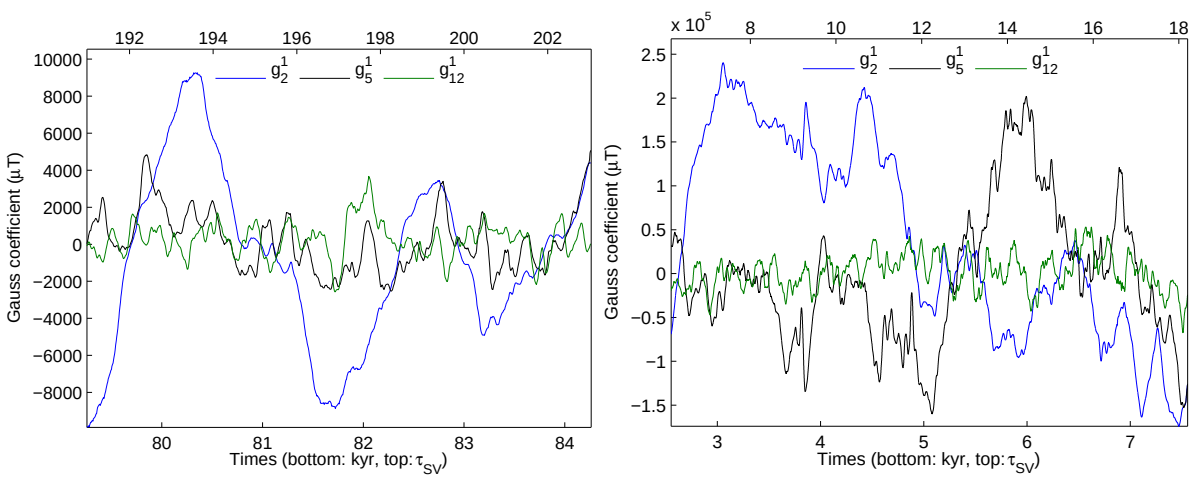

Figure 2. 5 kyr time series of coefficients $\mathcal{G}_2^1$, $\mathcal{G}_5^1$ and $\mathcal{G}_{12}^1$ from simulations CE (left) and S1 (right). The top scale gives the dimensionless time (based on τ_{SV}).

instead for $\gamma = 1$ in joint analyses of geodynamo simulations and geomagnetic field models. The latter authors also scaled time in simulations so that $\tau_{SV} = \delta|_{\gamma=1}$ matches the geophysical value and estimated $\tau_{SV} = 415$ years from a fit of τ_n for degrees $n \in [2 - 13]$.

Building on these works, we shall assume $\beta = \gamma = 1$ hence a flat spatial power spectrum R_n at the CMB for the observable length-scales. This simplification allows to easily convert numerical times into years. The remaining parameters (α, δ) entering equations (16) can be derived from the average of R_n and a least-squares fit of $\log(\tau_n)$ versus $\log(n)$. Since these two quantities are not normally distributed, a more accurate estimate may be obtained using a maximum likelihood approach, as developed by Lhuillier et al. (2011b) for τ_n (see appendix A). We discuss in Appendix B the estimation of the parameters of the regression model (16) as the conditions $\beta = \gamma = 1$ are relaxed.

For each simulation, we have computed different estimates of the spatial power spectrum R_n and of the time τ_n: an ensemble of instantaneous values $(\hat{R}_n, \hat{\tau}_n)$ averaged over m $(0 \leq m \leq n)$ only, an estimate $(\overline{R}_n, \overline{\tau}_n)$ averaged over m and the total duration of the simulations, and the similarly averaged (R_n^*, τ_n^*) once subtracted the mean values of the coefficients. Time-averaged estimates $(\overline{R}_n, \overline{\tau}_n \times n)$ and $(R_n^*, \tau_n^* \times n)$ are shown in Fig. 3 for the three simulations. We also represent the fits $R_n = \alpha$ and $\tau_n \times n = \delta$ calculated either with the least-square method or the maximum likelihood one. In addition, we plot two-sigma intervals for α and δ deduced from an ensemble of ten snapshots. Overall, the different time-averaged estimates of α and δ yield rather similar results given the large variability within the ensemble of snapshot estimates. Removing or not the average appears therefore as a secondary issue.

Spectra R_n for CE and S0 simulations are almost flat, validating the hypothesis $\beta = 1$, while that for the most extreme (lowest viscosity, strongest forcing) simulation S1 presents a slightly decreasing trend with n, closer to current estimates from geomagnetic field models, as further discussed in Appendix B.

Times τ_n reflect slightly different behaviors in all three simulations. If the hypothesis $\gamma = 1$ agrees well with the outputs from CE, S1 (resp. S0) favors instead a slightly larger (resp. lower) exponent. In simulation S1, we obtain a γ value closer to 1 after removing the time-average value of the coefficients, which mainly affects τ_n estimates at low degrees. Furthermore, we note a wide time variability in the instantaneous estimates $\hat{\tau}_n$, suggesting that a snapshot estimate alone, as available from modern geophysical observations (see e.g. Holme et al. 2011) for which the long-term average of coefficients is not available, is insufficient to determine precisely γ. All in all, we conclude that the simple hypothesis $\gamma = 1$ is consistent with our three simulations (see Appendix B for more details). An error of the order of 50% may occur when measuring the magnitudes of α and δ from instantaneous values, as shown by the two-sigma interval in Fig. 3 (right) and in table A2. This translates into a

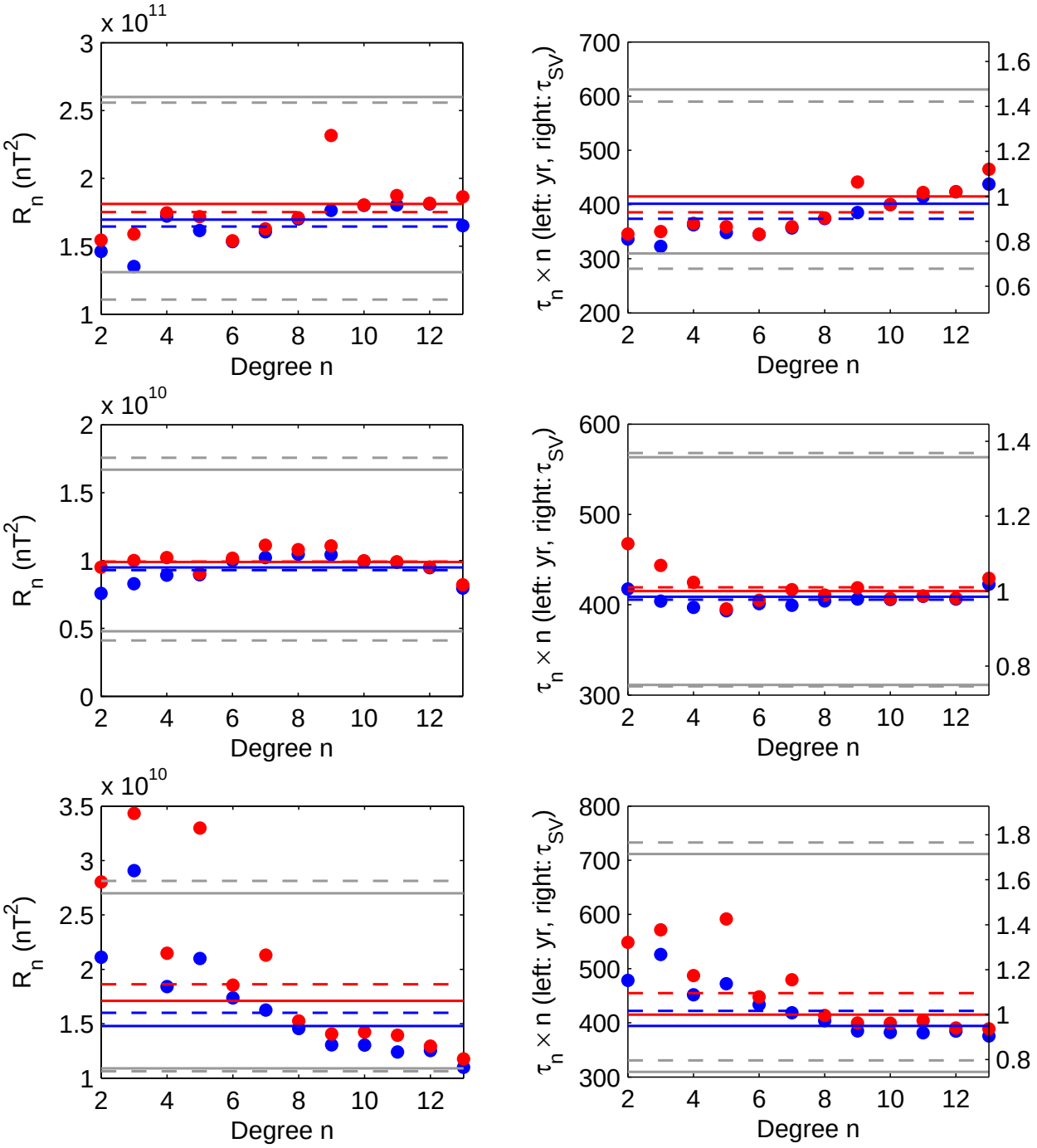

Figure 3. Spatial power spectrum R_n (left) and $n \times \tau_n$ (right) as a function of the spherical harmonic degree n for simulations S0 (top), CE (middle) and S1 (bottom) from the expected variances as in equation (15), either removing (blue dots) or keeping (red dots) the time-average of the coefficients. Dashed (resp. solid) colored lines stand for estimates of α and δ using least-squares (resp. maximum likelihood) regressions (16) with $\beta = \gamma = 1$. Grey lines represent the two-sigma intervals around the average of 10 estimates of α and δ from independent snapshots $\hat{R}_n$ and $\hat{\tau}_n$, which are not represented. The right scale on the $n \times \tau_n$ plots gives the dimensionless time in τ_{SV} units.

variability in τ_{SV} significantly larger than that observed by Lhuillier et al. (2011b) from a dynamo simulation at larger viscosity and lower forcing.

Note that the time-series of non-dipole coefficients represented on Fig. 2 appear uncorrelated when sampled over periods longer than $2\pi\tau_n = 2\pi\tau_{SV}/n$ (i.e. for periods longer than about 1300 yr, 500 yr, and 200 yr for degrees 2, 5, and 12 respectively). This suggests a flat power spectrum at lower frequencies, as expected for the two-parameter AR2 processes described in section 2.2

3.3 Frequency spectra of Gauss coefficients

In order to avoid frequency leakage when estimating the power spectrum for the finite-length time-series of Gauss coefficients, we adopt a multi taper approach (e.g., Percival and Walden 1993). The advantage of this approach is that the power spectrum variance is reduced by averaging independent estimates of the power spectrum obtained after multiplying the series by various orthogonal tapers. Several variants of the multi taper approach have been used before to assess the power spectrum of the dipole moment. Constable and Johnson (2005) relied on sine tapers (Riedel and Sidorenko 1995). Olson et al. (2012) chose instead to break the series into overlapping segments tapered using a Hanning window (Welch 1967). As Buffett and Matsui (2015), we adopt in this study an approach based on Slepian functions (Thomson 1982). We use seven Slepian tapers characterized by a power spectrum with energy concentrated in a bandwidth $[-W, W]$, where $W = 4/(N\Delta t)$, N is the number of data, and Δt is the sampling interval. As a consequence, the power spectrum estimated at a given frequency f is controlled by values of the power spectrum within $[f - W, f + W]$, with W the resolution of the power spectrum.

We test the multi taper approach of Thomson (1982) on a realisation of a stochastic process. The obtained spectra are further smoothed by running averages over a length that linearly increases with the frequency (from 1 point at minimum frequency to 201 points at maximum frequency). We show the spectra obtained for this realisation both before and after removing its averaged value (Fig. 4). Although these power spectra include a certain amount of noise, they reproduce well both the amplitude and the spectral indices of the true power spectrum, except at frequencies lower than the resolution W. At frequencies $f < W$, the average value of the series influences the power spectra, which strongly differ whether the average is removed or not: the spectrum obtained without removing the average shows a step at low frequencies, which is an artefact. The above method for calculating spectra is used below for all our results. Note that we do not remove linear trends in the time-series before computing the spectra. Nevertheless, we checked that the shape of the spectra computed here with the multi taper approach is not significantly different whether the trend has been removed or not.

Fig. 5 displays power spectra for degree 5 Gauss coefficient time series at the CMB, from the three

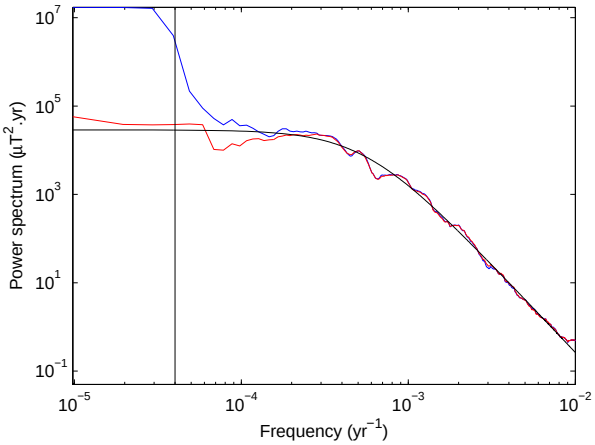

Figure 4. Comparison of power spectra for random time-series, estimated using the multi taper approach applied before (blue) and after (red) removing the averaged value of the series, and superimposed on the theoretical power spectrum (black). The series parameters are chosen to mimic a plausible behavior for the axial dipole coefficient (at the Earth's surface): it is a Gaussian random series with an averaged value of -35 μT, a standard deviation of 5 μT, with a two-parameters AR2 auto-covariance function as defined in equation (13), with $\omega^{-1} =$ 500 yrs. The theoretical power spectra of this series is given in equation (12). The series contains $N = 2000$ data sampled every $\Delta t = 50$ years. The vertical black line indicates the value of the concentration half-bandwidth $W = 4/(N\Delta t)$ of the Slepian tapers. These spectra were obtained using the subroutine pmtm from Matlab® and then further smoothed using running averages.

simulations. For the two longest simulations (S0 and CE), we observe that spectra for all coefficients are flat (or white) at low frequencies, and show a constant spectral index at high frequencies, hinting to a scale invariance. The change of spectral index occurs within a narrow band of frequencies, and the cut-off frequency between the two regions of the spectra increases with the spherical harmonic degree, as illustrated in Fig. 6 for the CE dynamo. Whereas the spectral index at large frequencies appears independent of the spherical harmonic order in S0, it significantly increases with m in the CE and S1 simulations. Power spectra obtained from S1 do not show a flat plateau at low frequencies as a consequence of the short duration of the simulation: we do not have access to long enough periods to reach the domain where $P \propto f^0$. Spectra for this simulation show a steep decrease with f at high frequency, which is absent in the S0 and CE spectra.

3.4 Comparison with the spectrum of a two-parameter AR2 process

Expression (13) corresponds to a particular autoregressive process of order 2 that only depends on two parameters, a variance σ^2 and a characteristic time-scale ω^{-1}. As in Gillet et al. (2013), we further assume that these two parameters only depend on the spherical harmonic degree n, which amounts to posit that the statistics of the field are independent of longitude and latitude (Hulot and Bouligand

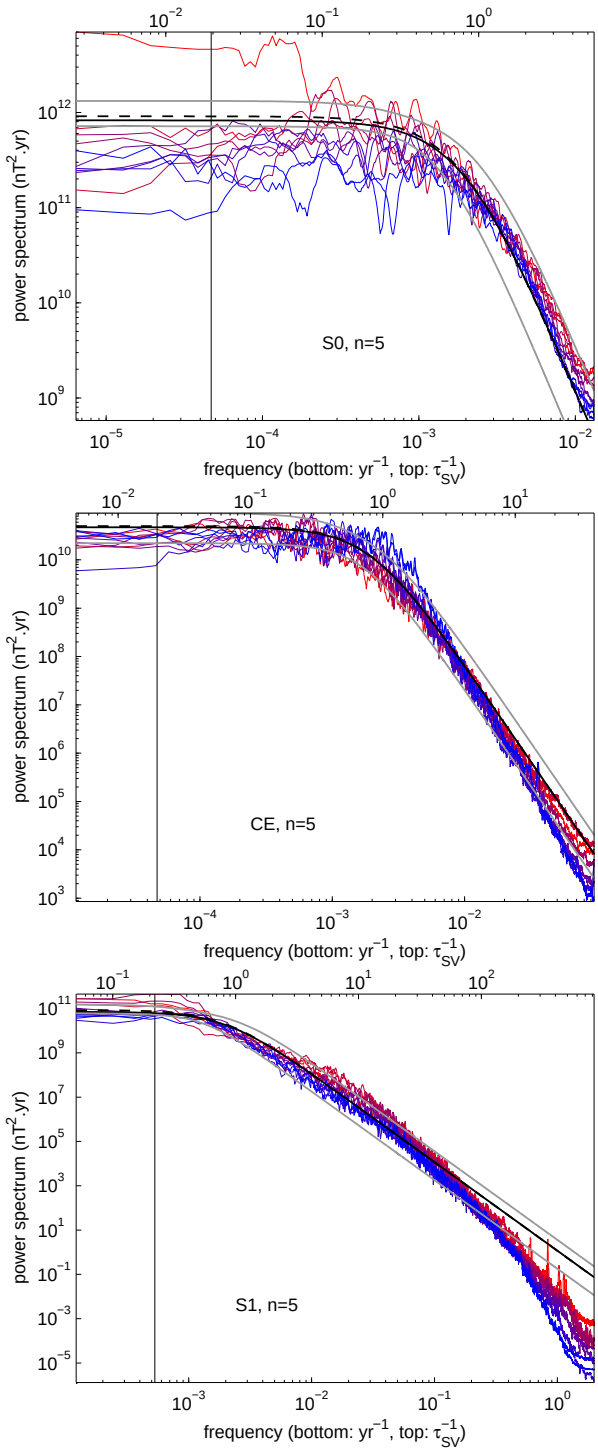

Figure 5. Power spectra computed using the multi taper approach of Thomson (1982) for coefficients of degree $n = 5$, from simulations S0 (top), CE (middle), and S1 (bottom). All coefficients $\mathcal{G}_n^m$ and $\mathcal{H}_n^m$ of order $m \in [0, n]$ are represented with gradually varying colors (from red for $m = 0$ to blue for $m = n$). The black solid (dashed) curves display the power spectra (12) with parameters τ_n and σ_n estimated using the maximum likelihood method and using time averaged Gauss coefficients variances in (15), once removed (or not) their averaged value. The grey lines represent the two-sigma interval around the average of 10 power spectra with parameters ω_n^{-1} and σ_n deduced from independent snapshot $\hat{R}_n$ and $\hat{\tau}_n$. The thin vertical black line indicates the resolution half-bandwidth. The top scale gives the dimensionless frequency (based on τ_{SV}^{-1}).

2005). Then, for each degree n, one deduces from (15) that $\sigma_n^2 = R_n/(n+1)(2n+1)$, and from equations (5) and (6) the relation $\omega_n^{-1} = \tau_n$; these two parameters define the auto-covariance functions $C_n(\tau)$.

Since long enough geophysical series to produce statistical averages are not available, Gillet et al. (2013) approximated (R_n, τ_n) by the quantity $(\hat{R}_n, \hat{\tau}_n)$ estimated from a snapshot of the well documented (and supposedly representative) satellite era. This approximation relies on the assumption that main field and secular variation series are unbiased, i.e. $E(\mathcal{G}_n^m) = E(\mathcal{H}_n^m) = E(\partial_t \mathcal{G}_n^m) = E(\partial_t \mathcal{H}_n^m) = 0$. This assumption is certainly not valid for the axial dipole between two polarity reversals. For this reason, Hellio et al. (2014) considered instead dipole deviations in the expression (15) for $n = 1$. We test here the validity of using snapshot estimate $(\hat{R}_n, \hat{\tau}_n)$ to define the auto-covariance function of non-dipole coefficients.

For each simulation, we estimate parameters α and δ entering (16) (with $\beta = \gamma = 1$) using both averaged and instantaneous estimates of the spatial power spectrum and correlation times (i.e., $(\bar{R}_n, \bar{\tau}_n)$, (R_n^*, τ_n^*) and $(\hat{R}_n, \hat{\tau}_n)$) and a maximum likelihood approach. α and δ are then used to determine variances σ_n^2 and correlation times ω_n^{-1}, and to predict the theoretical spectrum (12) for all degrees n. We then estimate a two-sigma interval from 10 spectra (12) deduced from snapshots. These curves are superimposed in Fig. 5 (for $n = 5$) and Fig. 6 (CE simulation for $n = 2, 5, 12$) on spectra of the Gauss coefficients.

For all three simulations and all degrees, we observe overall a good agreement between the different theoretical spectra, with some discrepancies that we detail in the next paragraph. The theoretical spectra obtained from averaged estimates once removed or not the coefficient averaged value are very close, suggesting that the assumption of unbiased series is valid. The two-sigma intervals are relatively narrow compared to the noise level in the individual spectra and to the variability among spectra of same degree, showing that the use of snapshot estimates is appropriate.

For simulation S0, the power-spectra calculated from (12) reproduce very well the power spectra of the field coefficients at all frequencies. For simulation CE, the spectrum (12) approximates relatively well the power spectra of low order Gauss coefficients for all degrees n. On the other hand, the power spectra for the largest order coefficients ($m \sim n$) decreases more rapidly than f^{-4} at its high frequency end. Simulation S1 also presents, at periods shorter than 10 years, Gauss coefficient power spectra steeper than f^{-4}. Buffett and Matsui (2015) conjecture that the occurrence of a period range presenting a $s = 6$ spectral index, as observed from numerical computations (Olson et al. 2012; Davies and Constable 2014), could be related with a mechanism involving magnetic diffusion below the CMB. However, the identification of a spectral index s requires a power-law behavior $P(f) \propto f^{-s}$ over a significant frequency range. Instead, a power spectrum $P(f) \propto \exp(-f)$, which is reminiscent of a

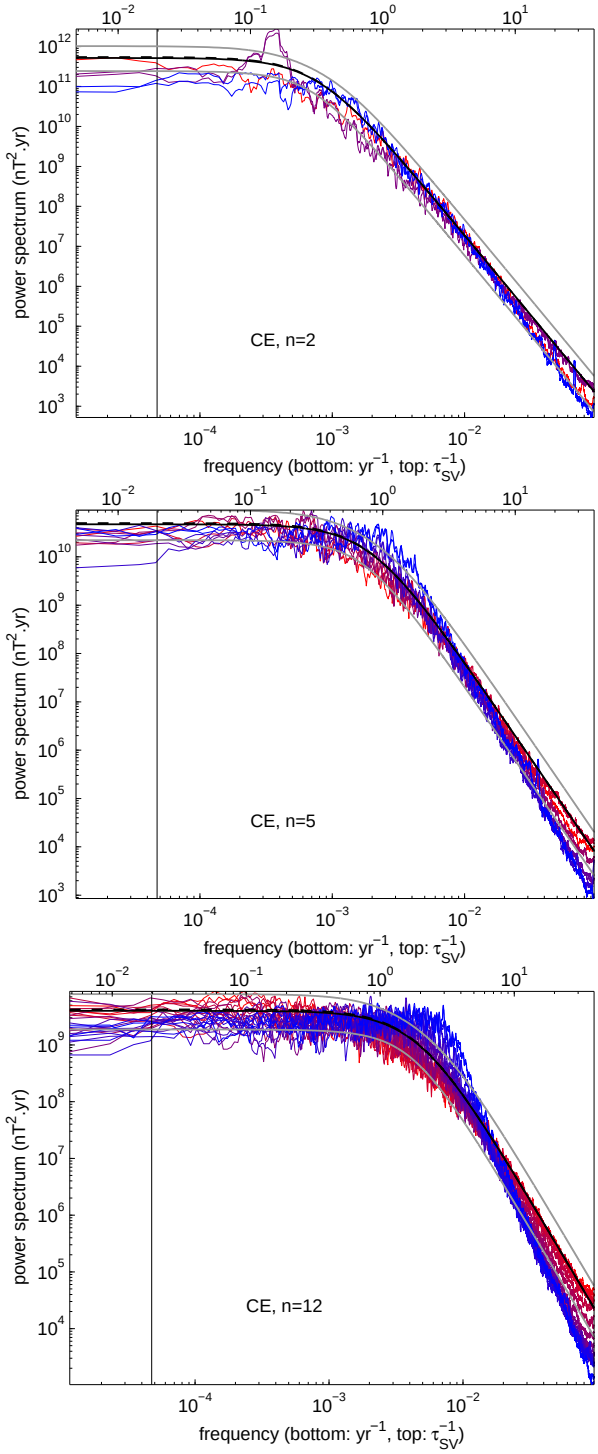

Figure 6. Power spectra for Gauss coefficients series of spherical harmonic degrees 2, 5 and 12, from the CE simulation. Same colors and line types as in Fig. 5.

dissipation range (see e.g. Frisch 1995), may arguably be observed at high frequencies in simulation S1. Hence, the narrow range of frequencies that displays a spectral index of 4 may result from too important diffusive processes in simulations (see §4.3).

4 DISCUSSION

4.1 Model for dipole fluctuations

The minimal model (12), which appears appropriate for all Gauss coefficients but the axial dipole in our simulations, involves only one time-scale ω^{-1}. It can be presented (see §2.1) as a special case ($\omega = \chi$, *i.e.* $\tau_s = \tau_f$) within a more general family of models (3) having two distinct time-scales ω^{-1} and χ^{-1} – or equivalently τ_s and τ_f, see equation (11). For $\omega < \chi$, the associated power spectra (3) show a power law in f^{-2} at intermediate frequencies – between frequencies $1/(2\pi\tau_s)$ and $1/(2\pi\tau_f)$. For this reason, they were employed by Buffett and Matsui (2015) to account for the spectrum of the axial dipole as inferred from numerical simulations and from geomagnetic models. We concur with these results. In the two simulations S0 and CE that are long enough to address long-lived dipole fluctuations, the power spectrum for the axial dipole coefficient $\mathcal{G}_1^0$ does not present a sharp transition from 0 to 4 spectral index (see Fig. 7). Contrary to the equatorial dipole coefficients $\mathcal{G}_1^1$ and $\mathcal{H}_1^1$, whose spectra are well fitted by a two parameters AR2 spectrum (12), the spectrum for $\mathcal{G}_1^0$ shows an intermediate spectral index over about one decade, which is well fitted by the three parameter function (3).

The calculation of τ_s and τ_f by Buffett and Matsui hinges on the determination of the two transition frequencies between domains of spectral index 4, 2, and 0 respectively (see §2.1). Fig. 7 illustrates our fit between the spectra for S0 and CE and the function (3) where we have entered our estimations for ω and χ (directly related to τ_s and τ_f). Table 2 gives a comparison between our results and the values of τ_s and τ_f calculated by Buffett and Matsui but scaled in units of τ_{SV}. In S0 and CE, the transition frequency between domains of spectral index $s \simeq 2$ and $s \simeq 4$ (Fig. 7) leads to $\tau_f \simeq 65$ and 125 yrs respectively, values about 2 to 3 times larger than the estimates by Buffett and Matsui. Switching to long periods, they made the analogy between the times τ_s and t_d found in their simulations. Although this analogy cannot be ruled out by our results, simulations S0 and CE show values of the ratio t_d/τ_s significantly different from 1 (see Tables 1 and 2).

Unfortunately, the frequency range with a flat power spectrum is clear neither in the simulations investigated here, nor in those of Buffett and Matsui. In both studies, this part of the power spectrum is within the concentration bandwidth of the taper (see their Fig. 4 and our Fig. 7); we thus cannot determine if this is to be associated with a real feature of the axial dipole power spectrum, or with

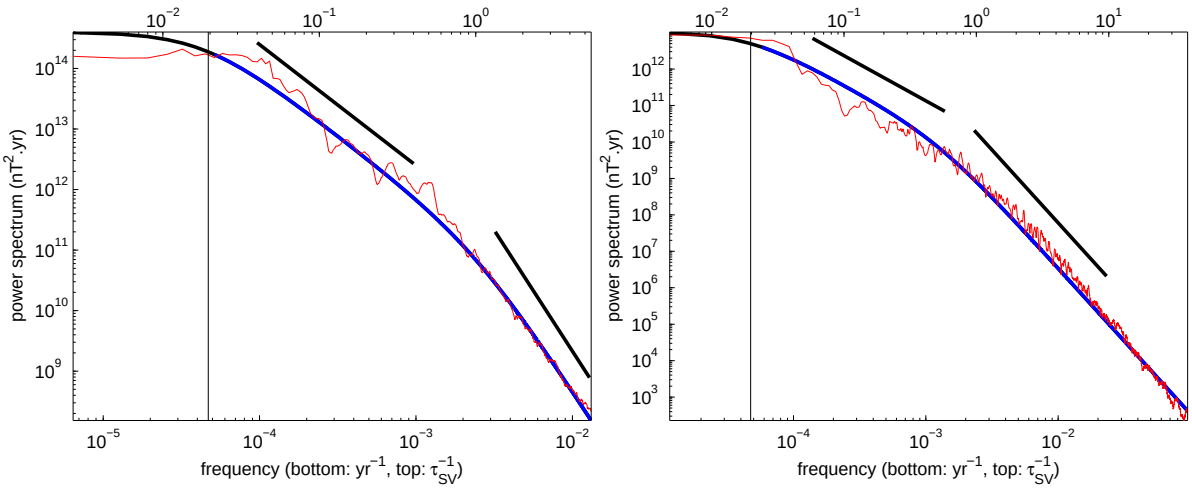

Figure 7. Power spectra (red) for the axial dipole series from simulations S0 (left), and CE (right). In black are superimposed the three parameters AR2 spectra (3) fitted to the series spectra for $f > W$ – range covered by the blue fit. The parameter W denotes the resolution half-bandwidth. The axial dipole variance is obtained directly from the series (removing the average). The frequency ω is estimated from the square root of the ratio of the variances of $\mathcal{G}_1^0$ and $\partial\mathcal{G}_1^0/\partial t$. The remaining parameter χ is obtained by minimizing the L2 norm of the difference between the logarithms of $\mathcal{G}_1^0$ series spectrum and of (3). The top scale gives the dimensionless frequency (based on τ_{SV}^{-1}). The thin vertical line indicates $f = W$. Black segments indicate spectral indices of 2 and 4.

an artefact due to tapering. As a result, the estimates of τ_s obtained from numerical simulations and given in Table 2 are not very accurate. Nevertheless, all estimates for $\omega^{-1} = (\tau_s\tau_f)^{1/2}$ obtained from numerical series of the axial dipole are within a factor of 2 of the value that we would obtain by extrapolating the relation $\omega_n^{-1} = \tau_n = \tau_{SV}/n$ (used for non-dipole coefficients) to the degree $n = 1$ (i.e., $\omega^{-1} = 415$ yr) .

The time ω^{-1} inferred from paleo- and archeomagnetic models appears significantly longer than estimates deduced from numerical simulations. In our opinion, the spectra of archeomagnetic field models, in the high frequency range where the spectral index is $s \simeq 4$, are much influenced by the regularization used in their construction. This explains why these models do not resolve geomagnetic jerks.

4.2 Deviations from spherical symmetry

Whereas temporal spectra from simulation S0 are fairly independent of the order m for all degrees but $n = 1$ (Fig. 5), suggesting that fluctuations of the non-dipole field are spherically symmetric at the CMB, we detect some significant dependence on the order from computations CE and S1. In CE, the spectra for coefficients of large order ($m \simeq n$) present a larger spectral index at high frequencies.

Model/Simulation	τ_s(yr)	τ_f(yr)	ω^{-1}(yr)	Reference
PADM2M$^{\dagger 1}$ - CALS10k.1b$^{\dagger 2}$	29 000	100-200	1700-2400	Buffett et al. (2013); Buffett and Matsui (2015)
Calypso (Rm=90)	1050	37	200	Buffett et al. (2014); Buffett and Matsui (2015)
Calypso (Rm=42)	1100	35	200	Buffett and Matsui (2015)
S0	3610	65	480	
CE	3490	125	660	

Table 2. Time-scales τ_s and τ_f involved to reproduce the power spectrum of the axial dipole deduced from archeo- and paleo-magnetic observations and from dynamo numerical simulations (see the definitions of τ_s and τ_f in equations (8) and (9) respectively). The time ω^{-1} is obtained as $(\tau_s\tau_f)^{1/2}$. The different times of the Calypso simulations have been converted into the τ_{SV}-based scaling adopted throughout the paper, using $t_d = Rm \times \tau_{SV}/14$ (Lhuillier et al. 2011a). $^{\dagger 1}$ Ziegler et al. (2011), $^{\dagger 2}$ Korte and Constable (2011).

As a consequence, more energy is contained in coefficients of small order at high frequencies and in coefficients of large order at intermediate frequencies (for periods typically from 100 to 1000 yrs). Because spherical harmonics of low and large orders have their largest contributions at respectively high and low latitudes, this suggests fluctuations at intermediate periods are stronger at low latitude (equatorial features primarily project into sectorial coefficients). This likely reflects the westward drift of low latitude structures observed in the CE simulation (see Aubert et al. 2013).

The power spectra for coefficients $\mathcal{G}_2^1$ and $\mathcal{H}_2^1$ in simulation CE (and to a lesser extent for order 1, degrees 4 and 6 coefficients, not shown) display a significant peak at periods around 2500 yrs (see Fig. 6), which translates into quasi-periodic oscillations in the time-series (see Fig. 1, right). This particular period corresponds to the time needed to circumnavigate the outer core at the average speed of the westward drift (Aubert et al. 2013). These periodic variations mainly affect $m = 1$ coefficients of the magnetic field through the advection of the eccentric gyre resulting, in the CE scenario, from the heterogeneous heat fluxes.

The topology of field patches at the CMB is influenced by the underlying dynamics. Indeed, the predominant Coriolis force in geodynamo simulations favors columnar structures aligned with the rotation axis, and together with magnetic forces it textures the vorticity field in the equatorial plane (e.g. Kageyama et al. 2008). As a result of field concentration by the vortices, the magnetic field at the CMB (outside the polar caps above and below the inner core) shows thin filaments primarily aligned along meridians (e.g. Takahashi and Shimizu 2012). This is illustrated in Fig. 8 for our lowest viscosity case, the strongly forced computation S1. We have thus some evidence that the Gauss coefficients at the core surface cannot be treated as independent variables.

We deduce the following consequences for the inversion of geomagnetic data. First, using an AR2 autocorrelation function that is independent of the coefficient order as prior information for the

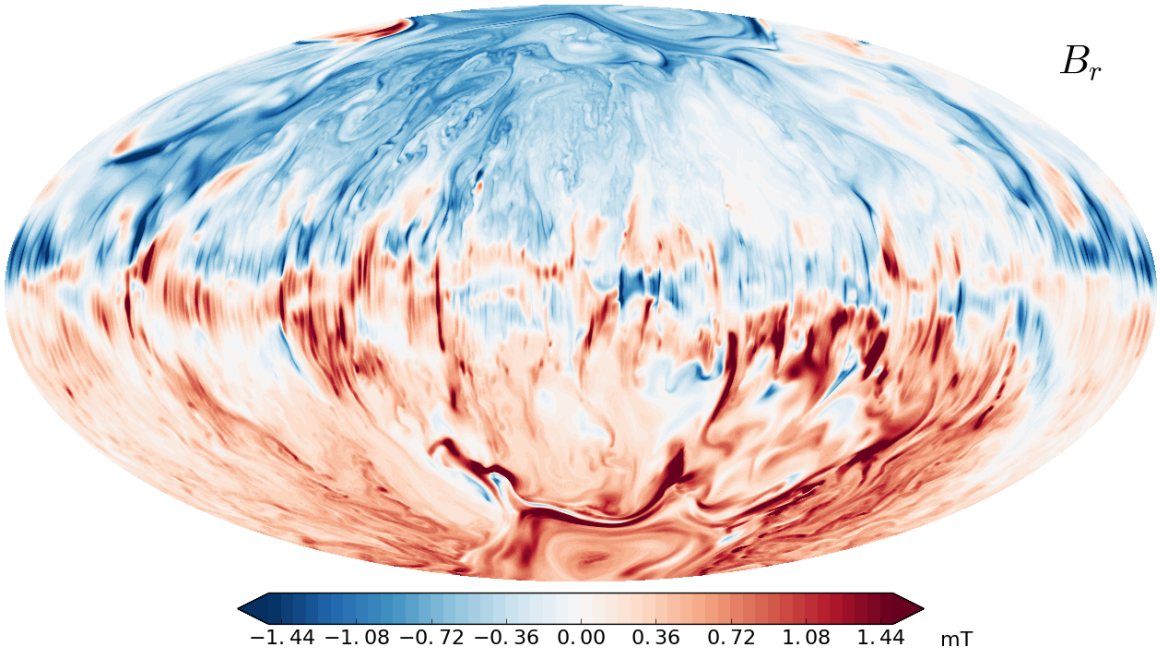

Figure 8. Full resolution snapshot of the radial magnetic field at the CMB for the S1 simulation, shown using an Aitoff projection. In this snapshot, the maximum intensity of the magnetic field at the CMB is about 7 mT.

inversion of geomagnetic models may penalize actual features of the geomagnetic field such as the westward drift of equatorial flux patches (Finlay and Jackson 2003) or periodic signals. Second, accounting for spatial cross-covariances (as performed with twin experiments on geodynamo simulations by Fournier et al. 2013) may improve the construction of prior information in field modeling studies.

4.3 Mechanisms underlying the different time-scales

Our approximation for the spectra of all coefficients but the axial dipole involves only one time-scale ω_n^{-1} $(= \tau_{SV}/n)$. Lhuillier et al. (2011a) argued that τ_{SV} is related to the advection time t_U, $\tau_{SV} \simeq 3t_U \simeq 14t_d/Rm$ (see table 1 for definitions) and this relationship holds within a factor of 2 in our simulations. This link between τ_{SV} and t_U suggests that the advection time, or eddy turnover time, controls the times ω_n^{-1}.

Our observation, from simulations S0 and CE, of a sharp transition between 0 and 4 spectral index ranges suggests that fluctuations of non-dipole coefficients are controlled by a single time-scale, or by two time-scales that are not significantly different. In our simulations, the axial dipole is the only coefficient for which we found necessary to consider AR2 processes defined with two distinct time-scales in order to account for the existence of a frequency range displaying a spectral index of 2. One could wonder as Buffett et al. (2013) whether this is to be related to the specificity of the axial dipole to show a non-zero average value. However, in this regard, our simulations may not

be representative of the Earth magnetic field. Indeed, differences between time-scales are smaller in simulations than they are for the Earth's core (see Table 1). In particular the ratio between the Alfvén time and the vortex turn-over time is about unity in simulations, instead of 10^{-2} in the Earth's core, which potentially shrinks the dynamics at periods between a few years and a few centuries in numerical computations. Therefore, if two time-scales were involved in the fluctuations of the Earth non dipole coefficients, these time-scales may be too close in simulations to be clearly distinguished. Relatively larger magnetic energy (and thus shorter Alfvén time) can be achieved in computations at Pm larger than unity (see e.g. Dormy 2016). Such computations unfortunately tend, at low Ekman numbers, to produce dynamos with Rm significantly lower than that of the Earth.

The simulation S1 covers a higher frequency range than S0 and CE. In this simulation, we observe that the spectrum becomes steeper than f^{-4} at periods shorter than a cutoff period $2\pi\tau \sim 3$ years (see Fig. 5 bottom). From the inspection of other spectra ($n \neq 5$, not shown), we find no evidence of the dependence of this cut-off time on the degree. Olson et al. (2012) also suggested, from dynamo simulations, a transition at high frequency towards a f^{-6} dependence in the axial dipole spectrum. They attributed this transition to the damping effect of the viscous layer beneath the outer boundary. Following these authors and interpreting the time τ as a magnetic dissipation time through a surface layer of thickness ϵ, i.e. $\tau = \epsilon^2/\eta = \pi^2 t_d \epsilon^2/c^2$, we find $\epsilon \sim 2\,10^{-3}c$. As a result, the thickness of the dissipative layer ϵ is found to be about three times the Ekman layer thickness, $E^{1/2}D$ (e.g., Greenspan 1968). Simulations differ from the geophysical situation inasmuch they are controlled by viscosity (King and Buffett 2013; Soderlund et al. 2012; Cheng and Aurnou 2016), with length-scales for viscous and magnetic dissipation being comparable. In a more Earth-like regime where viscosity is negligible, we can expect a dissipation cutoff at higher frequency associated to a thinner dissipative layer. We have indeed no evidence of a cut-off period from geomagnetic observations (Finlay et al. 2013).

4.4 Concluding remarks

The two sketchs presented in Fig. 9 summarize our interpretation of the coefficients power spectra, relating the cut-off periods between domains with different spectral indices to several characteristic time-scales.

The analysis of our simulations indicates that the spectra of simple two-parameters AR2 processes, calibrated by instantaneous values of R_n and τ_n, provide a good approximation of the spectra of all individual Gauss coefficients but the axial dipole. Although the axial dipole requires a more sophisticated AR2 process to account for the spectral index of 2 observed at millennial and longer periods, the use of a two-parameters process may still be sufficient for the construction of geomagnetic models.

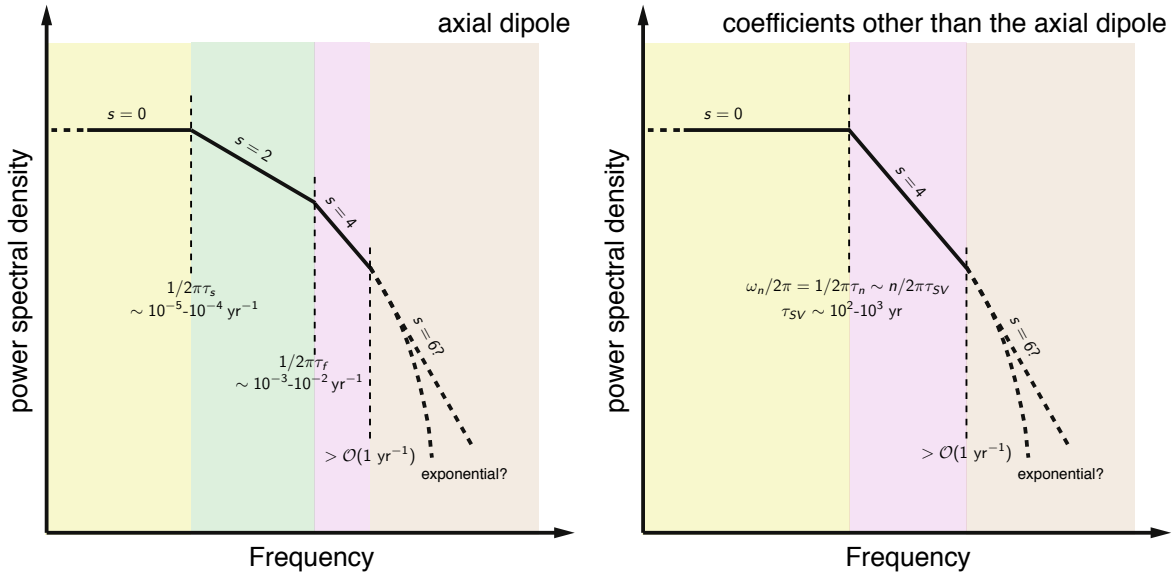

Figure 9. Schematic view of the power spectrum for the axial dipole (left) and non-dipole (right) coefficients. We associate the cut-off frequencies between domains of different spectral indices to several typical time-scales. Note that there is a factor of 2π between the cut-off periods in the power spectra and the time-scales τ_s and τ_f of equation (11).

Indeed, prior information is mainly needed to quantify the high frequency variability of the coefficients (Hellio et al. 2014). In particular, the axial dipole being well constrained by measurements, the behavior of its prior at low frequency does not matter much.

Previous to this work, it was already known that there is a good agreement for the spectrum of the axial dipole between simulations and observations (Buffett and Matsui 2015). Assuming that this correspondence holds for the other field coefficients, we end up with a prescription for the prior needed to model the observed field, namely the covariance function (13) in the non-dipolar case.

5 ACKNOWLEDGMENTS

This work was motivated and initiated during Gabrielle Hellio's PhD thesis whose purpose was to build new Bayesian models of the archeomagnetic field incorporating realistic a priori covariances describing the temporal behavior of Gauss coefficients. We thank anonymous referees for their comments that helped improve the organisation and clarity of our manuscript. This work was supported by the French Agence Nationale de la Recherche under the grant ANR-2011-BS56-011 (ANR AVSGEOMAG). The XSHELLS code is freely available at `https://bitbucket.org/nschaeff/xshells`. Numerical simulations were run on HPC resources from PRACE and GENCI at Curie/TGCC (Grants 2010PA1039, 2010PA1413, t2014047258), on the S-CAPAD platform (IPGP, France) and on the

Froggy platform of the CIMENT infrastructure (`https://ciment.ujf-grenoble.fr`), supported by the Rhône-Alpes region (GRANT CPER07_13 CIRA), the OSUG@2020 Labex (reference ANR10 LABX56) and the Equip@Meso project (reference ANR-10-EQPX-29-01). ISTerre is part of Labex OSUG@2020 (ANR10 LABX56). This is IPGP contribution xxxx.

REFERENCES

Aubert, J., 2015. Geomagnetic forecasts driven by thermal wind dynamics in the Earth's core. Geophys. J. Int. 203, 1738–1751.

Aubert, J., Aurnou, J., Wicht, J., 2008. The magnetic structure of convection-driven numerical dynamos. Geophys. J. Int. 172, 945–956.

Aubert, J., Finlay, C.C., Fournier, A., 2013. Bottom-up control of geomagnetic secular variation by the Earth's inner core. Nature 502, 219–223.

Backus, G., Parker, R., Constable, C., 1996. Foundations of geomagnetism. Cambridge University Press, Cambridge (UK).

Brendel, K., Kuipers, J., Barkema, G., Hoyng, P., 2007. An analysis of the fluctuations of the geomagnetic dipole. Phys. Earth planet. Int. 162, 249–255.

Brown, W.J., 2015. Observations and characterisation of rapid variations in the Earth's internal magnetic field. Ph.D. thesis. University of Leeds.

Buffett, B., 2015. Dipole fluctuations and the duration of geomagnetic polarity transitions. Geophys. Res. Lett. 42, 7444–7451.

Buffett, B., Matsui, H., 2015. A power spectrum for the geomagnetic dipole moment. Earth planet. Sci. Lett. 411, 20–26.

Buffett, B.A., King, E.M., Matsui, H., 2014. A physical interpretation of stochastic models for fluctuations in the Earth's dipole field. Geophys. J. Int. 198, 597–608.

Buffett, B.A., Ziegler, L., Constable, C.G., 2013. A stochastic model for palaeomagnetic field variations. Geophys. J. Int. 195, 86–97.

Cheng, J., Aurnou, J., 2016. Tests of diffusion-free scaling behaviors in numerical dynamo datasets. Earth planet. Sci. Lett. 436, 121–129.

Christensen, U.R., Aubert, J., 2006. Scaling properties of convection-driven dynamos in rotating spherical shells and application to planetary magnetic fields. Geophys. J. Int. 166, 97–114.

Christensen, U.R., Tilgner, A., 2004. Power requirements of the geodynamo from ohmic losses in numerical and laboratory dynamos. Nature 429, 169–171.

Christensen, U.R., Wardinski, I., Lesur, V., 2012. Timescales of geomagnetic secular acceleration in satellite field models and geodynamo models. Geophys. J. Int. 190, 243–254.

Constable, C., Johnson, C., 2005. A paleomagnetic power spectrum. Phys. Earth Planet. Int. 153, 61–73.

Constable, C., Parker, R., 1988a. Smoothing, splines and smoothing splines; their application in geomagnetism. J. Comput. Phys. 78, 493–508.

Constable, C.G., Parker, R.L., 1988b. Statistics of the geomagnetic secular variation for the past 5 m.y. J. Geophys. Res. 93, 11569–11581.

Davies, C.J., Constable, C.G., 2014. Insights from geodynamo simulations into long-term geomagnetic field behaviour. Earth planet. Sci. Lett. 404, 238–249.

De Santis, A., Barraclough, D., Tozzi, R., 2003. Spatial and temporal spectra of the geomagnetic field and their scaling properties. Phys. Earth Planet. Int. 135, 125–134.

Dormy, E., 2016. Strong-field spherical dynamos. J. Fluid Mech. 789, 500–513. doi:10.1017/jfm.2015.747.

Finlay, C.C., Jackson, A., 2003. Equatorially dominated magnetic field change at the surface of Earth's core. Science 300, 2084–2086.

Finlay, C.C., Olsen, N., Gillet, N., Jault, D., 2013. Rapid core field variations during the satellite era: investigations using stochastic processes based field models. AGU Fall meeting.

Fournier, A., Aubert, J., Thébault, E., 2015. A candidate secular variation model for IGRF-12 based on Swarm data and inverse geodynamo modelling. Earth, Planets and Space 67, 81.

Fournier, A., Nerger, L., Aubert, J., 2013. An ensemble Kalman filter for the time-dependent analysis of the geomagnetic field. Geochem. Geophys. Geosyst. 14, 4035–4043.

Frisch, U., 1995. Turbulence: the legacy of AN Kolmogorov. Cambridge University Press, Cambridge (UK).

Gardiner, C.W., 1985. Handbook of stochastic methods for physics, chemistry and the natural sciences. Springer, Berlin.

Gillet, N., Barrois, O., Finlay, C., 2015. Stochastic forecasting of the geomagnetic field from the COV-OBS.x1 geomagnetic field model, and candidate models for IGRF-12. Earth, Planets and Space 67, 71. doi:10.1186/s40623-015-0225-z.

Gillet, N., Jault, D., Canet, E., Fournier, A., 2010. Fast torsional waves and strong magnetic field within the Earth's core. Nature 465, 74–77.

Gillet, N., Jault, D., Finlay, C.C., Olsen, N., 2013. Stochastic modelling of the Earth's magnetic field: inversion for covariances over the observatory era. Geochem. Geophys. Geosyst. 14, 766–786.

Greenspan, H.P., 1968. The theory of rotating fluids. CUP Archive.

Hellio, G., 2015. Stochastic modeling of archeomagnetic measurements. Ph.D. thesis. Université Grenoble Alpes. URL: `https://tel.archives-ouvertes.fr/tel-01218123`.

Hellio, G., Gillet, N., Bouligand, C., Jault, D., 2014. Stochastic modelling of regional archaeomagnetic series. Geophys. J. Int. 199, 931–943.

Holme, R., Olsen, N., 2006. Core surface flow modelling from high-resolution secular variation. Geophys. J. Int. 166, 518–528.

Holme, R., Olsen, N., Bairstow, F., 2011. Mapping geomagnetic secular variation at the core–mantle boundary. Geophys. J. Int. 186, 521–528.

Hulot, G., Bouligand, C., 2005. Statistical palaeomagnetic field modelling and symmetry considerations.

Geophys. J. Int. 161, 591–602.

Hulot, G., Le Mouël, J., 1994. A statistical approach to the Earth's main magnetic field. Phys. Earth planet. Int. 82, 167–183.

Jackson, A., Jonkers, A.R.T., Walker, M.R., 2000. Four centuries of geomagnetic secular variation from historical records. Phil. Trans. R. Soc. Lond. A 358, 957–990.

Jazwinski, A.H., 2007. Stochastic processes and filtering theory. Dover Publications, Mineola.

Kageyama, A., Miyagoshi, T., Sato, T., 2008. Formation of current coils in geodynamo simulations. Nature 454, 1106–1109.

King, E.M., Buffett, B.A., 2013. Flow speeds and length scales in geodynamo models: The role of viscosity. Earth planet. Sci. Lett. 371, 156–162.

Korte, M., Constable, C., 2011. Improving geomagnetic field reconstructions for 0–3 ka. Phys. Earth planet. Int. 188, 247 – 259.

Korte, M., Donadini, F., Constable, C., 2009. Geomagnetic field for 0-3 ka: 2. A new series of time-varying global models. Geophys. Geochem. Geosyst. 10. doi:10.1029/2008GC002297.

Kuipers, J., Hoyng, P., Wicht, J., Barkema, G., 2009. Analysis of the variability of the axial dipole moment of a numerical geodynamo model. Phys. Earth planet. Int. 173, 228–232.

Lesur, V., Wardinski, I., Rother, M., Mandea, M., 2008. GRIMM: the GFZ Reference Internal Magnetic Model based on vector satellite and observatory data. Geophys. J. Int. 173, 382–394.

Lhuillier, F., Aubert, J., Hulot, G., 2011a. Earth's dynamo limit of predictability controlled by magnetic dissipation. Geophys. J. Int. 186, 492–508.

Lhuillier, F., Fournier, A., Hulot, G., Aubert, J., 2011b. The geomagnetic secular-variation timescale in observations and numerical dynamo models. Geophys. Res. Lett. 38, L09306. doi:10.1029/2011GL047356.

Lowes, F., 1974. Spatial power spectrum of the main geomagnetic field, and extrapolation to the core. Geophys. J. R. astr. Soc. 36, 717–730.

MacKay, 1998. Introduction to Gaussian processes, in: Bishop, C.M. (Ed.), Neural networks and machine learning, Springer, Berlin. pp. 133–165.

Mandea, M., Holme, R., Pais, A., Pinheiro, K., Jackson, A., Verbanac, G., 2010. Geomagnetic jerks: rapid core field variations and core dynamics. Space science reviews 155, 147–155.

Meduri, D.G., Wicht, J., 2016. A simple stochastic model for dipole moment fluctuations in numerical dynamo simulations. Front. Earth Sci. 4, 38.

Olson, P., Christensen, U., Driscoll, P., 2012. From superchrons to secular variation: A broadband dynamo frequency spectrum for the geomagnetic dipole. Earth planet. Sci. Lett. 319-320, 75–82.

Panovska, S., Finlay, C., Hirt, A., 2013. Observed periodicities and the spectrum of field variations in Holocene magnetic records. Earth planet. Sci. Lett. 379, 88–94.

Percival, D.B., Walden, A.T., 1993. Spectral Analysis for Physical Applications: Multitaper and Conventional Univariate Techniques. Cambridge University Press, Cambridge.

Riedel, K.S., Sidorenko, A., 1995. Minimum bias multiple taper spectral estimation. IEEE Transactions on

Signal Processing 43, 188–195.

Roberts, P., Jones, C., Calderwood, A., 2003. Energy fluxes and ohmic dissipation in the earth's core, in: Jones, C., Soward, A., Zhang, K. (Eds.), Earth's core and lower mantle. Taylor & Francis, London, pp. 100–129.

Schaeffer, N., 2013. Efficient spherical harmonic transforms aimed at pseudospectral numerical simulations. Geochem. Geophys. Geosyst. 14, 751–758.

Schaeffer, N., 2015. Exploring the physics of the Earth's core with numerical simulations. Habilitation à diriger des recherches. Université Grenoble Alpes. URL: `https://tel.archives-ouvertes.fr/tel-01241755`.

Soderlund, K.M., King, E.M., Aurnou, J.M., 2012. The influence of magnetic fields in planetary dynamo models. Earth planet. Sci. Lett. 333, 9–20.

Takahashi, F., Shimizu, H., 2012. A detailed analysis of a dynamo mechanism in a rapidly rotating spherical shell. J. Fluid Mech. 701, 228–250.

Tanriverdi, V., Tilgner, A., 2011. Global fluctuations in magnetohydrodynamic dynamos. New Journal of Physics 13, 033019.

Thébault, E., Gallet, Y., 2010. A bootstrap algorithm for deriving the archeomagnetic field intensity variation curve in the Middle East over the past 4 millennia BC. Geophys. Res. Lett. 37, L22303. doi:10.1029/2010GL044788.

Thomson, D.J., 1982. Spectrum estimation and harmonic analysis. Proceedings of the IEEE 70, 1055–1096.

Van Kampen, N.G., 2007. Stochastic processes in physics and chemistry. Elsevier, Amsterdam.

Welch, P., 1967. The use of fast Fourier transform for the estimation of power spectra: a method based on time averaging over short, modified periodograms. IEEE Transactions on audio and electroacoustics , 70–73.

Yaglom, A.M., 2004. An introduction to the theory of stationary random functions. Dover Publications, Mineola.

Ziegler, L., Constable, C., Johnson, C., Tauxe, L., 2011. PADM2M: a penalized maximum likelihood model of the 0–2 Ma palaeomagnetic axial dipole moment. Geophys. J. Int. 184, 1069–1089.

APPENDIX A: MAXIMUM LIKELIHOOD ESTIMATION OF LAW PARAMETERS FOR τ_N AND R_N

Within the maximum likelihood approach developed by Lhuillier et al. (2011b), the Gauss coefficients are assumed to be the result of a random Gaussian stationary process with a zero mean and a variance that depends only on the degree n. Given these assumptions, Lhuillier et al. (2011b) showed that the quantity $(\tau_n/\bar{\tau}_n)^2$ follows an F-distribution (also known as a Fisher-Snedecor distribution) with $((2n+1)N_n, (2n+1)N_n)$ degrees of freedom, noted $F^{(2n+1)N_n,(2n+1)N_n}$, with $\bar{\tau}_n$ the expectation of the time-scale τ_n and N_n the number of independent values in the Gauss coefficient time-series. N_n is equal to 1 when τ_n is estimated from an instantaneous model or a model covering a time-period shorter

than $3\tau_n$. N_n equals $T/(3\bar{\tau_n})$ for time-series of duration T longer than $3\tau_n$. Following Lhuillier et al. (2011b), the probability of a law (δ, γ) given the observed time-scale τ_n^{obs} for degrees N_0 to N is :

$$f(\delta,\gamma) = \prod_{n=N_0}^{N} F^{(2n+1)N_n,(2n+1)N_n}\left[\left(\frac{\tau_n^{obs}}{\delta n^{-\gamma}}\right)^2\right] \tag{A.1}$$

Because the likeliest value of the probability density function $F^{K,K}$ is $(K-2)/(K+2)$ for $K > 2$, the maximum likelihood estimate of (δ, γ) are the parameters that provide the maximum value of :

$$f(\delta,\gamma) = \prod_{n=N_0}^{N} F^{(2n+1)N_n,(2n+1)N_n}\left[\frac{(2n+1)N_n-2}{(2n+1)N_n+2}\left(\frac{\tau_n^{obs}}{\delta n^{-\gamma}}\right)^2\right] \tag{A.2}$$

The parameters (α, β) of equation 16 can be estimated using a similar approach. Within the assumptions of Lhuillier et al. (2011b), the quantity $(2n+1)R/\bar{R}_n$ follows a χ^2-distribution with $(2n+1)N_n$ degrees of freedom, noted $G^{(2n+1)N_n}$. The likeliest value of the χ^2 probability density function G^K is $K-2$ for $K > 2$. Therefore, the maximum likelihood estimate of (α, β) are the parameters that provide the maximum value of :

$$f(\alpha,\beta) = \prod_{n=N_0}^{N} G^{(2n+1)N_n}\left[((2n+1)N_n-2)\,\frac{R^{obs}}{\alpha\beta^n}\right] \tag{A.3}$$

The probability density functions defined in (A.3) and (A.2) and shown in Fig. A1 and A2 for simulation S0 display a single maximum showing that this method provides a unique result. Note however that the parameter spaces delimited by the contour lines of the probability density functions deduced from the different estimates may not overlap. This is the case for the two averaged estimates of τ_n (Fig. A1a and A1b) suggesting that the assumption of zero mean for the Gauss coefficients is not correct. The contour lines are elongated in an oblique direction showing that errors on parameters are correlated (errors on one parameter can be compensated by errors on the other parameters). As expected, the parameter space delimited by the contour lines is larger when using the instantaneous estimates of $\hat{R}_n$ and $\hat{\tau}_n$, which emphasizes that the estimated law is in this case less accurate.

APPENDIX B: RELAXING THE HYPOTHESES $\beta = 1$ AND $\gamma = 1$

Fits of R_n and τ_n in §3.2 have been obtained assuming the restricting hypothesis $\beta = \gamma = 1$ in equation (16). Here, we discuss how those regressions are modified once relaxing these constraints. This test is motivated by the derivation, from current geomagnetic field models, of larger (resp. lower) values for γ (resp. β). In particular, regression of τ_n from recent geomagnetic field models for degrees $n \geq 3$ gives $\gamma \simeq 1.45$ (Holme and Olsen 2006). A slightly lower value is obtained when including degree 2 in the regression.

For all estimates of R_n and τ_n and each simulation, we searched for the parameters (α, β) and

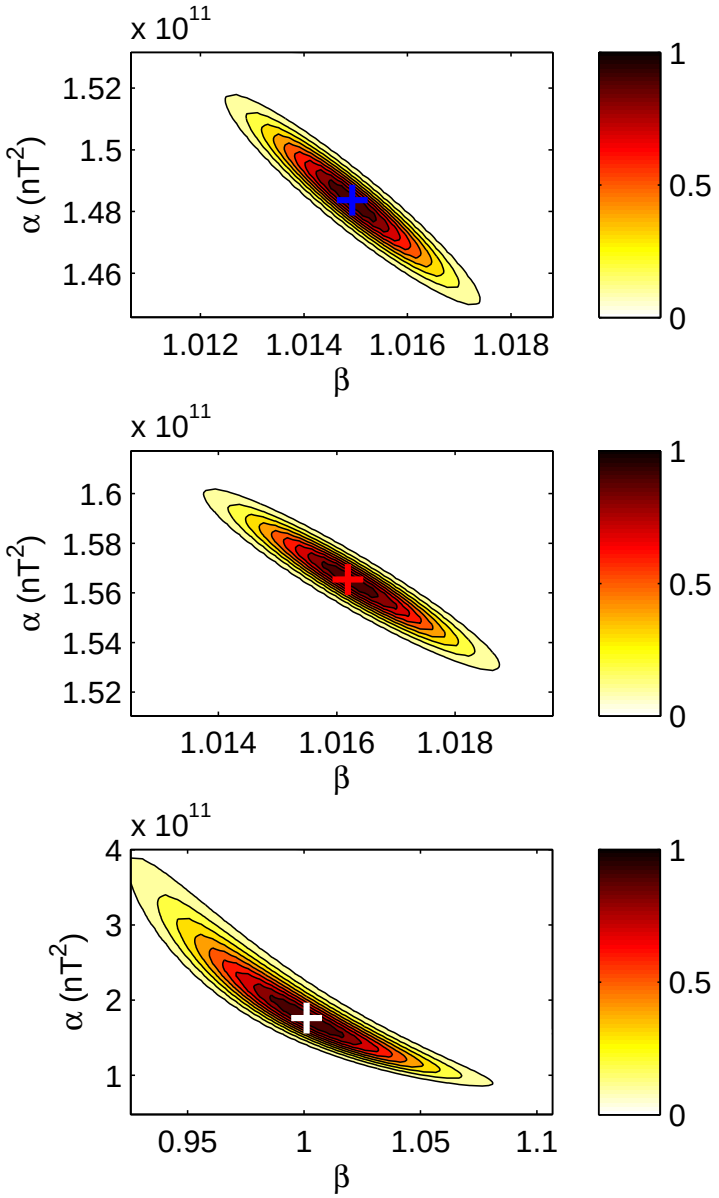

Figure A1. Probability density functions (normalized by their maximum value) for values of α and β (see equation 16) for the S0 simulation deduced from R_n^* estimated using Gauss coefficients after subtracting their averaged value (top), from $\bar{R}_n$ using original Gauss coefficients (middle), and from an instantaneous $\hat{R}_n$ (bottom). Crosses indicate the maximum likelihood parameters.

(δ, γ) from equation (16) for $n \in [2, 13]$. We used both the least-squares and the maximum likelihood methods. Results of the parameter search are summarized in Tables A1 and A2 and Fig. A3. As already observed by Lhuillier et al. (2011b), the results from the least-squares inversion and the maximum likelihood approach do not differ much.

The three simulations, run for different dimensionless parameters, provide different values of (α, β) and (δ, γ). Both S0 and CE show almost flat CMB spectra ($\beta \simeq 1$), whereas R_n is slightly

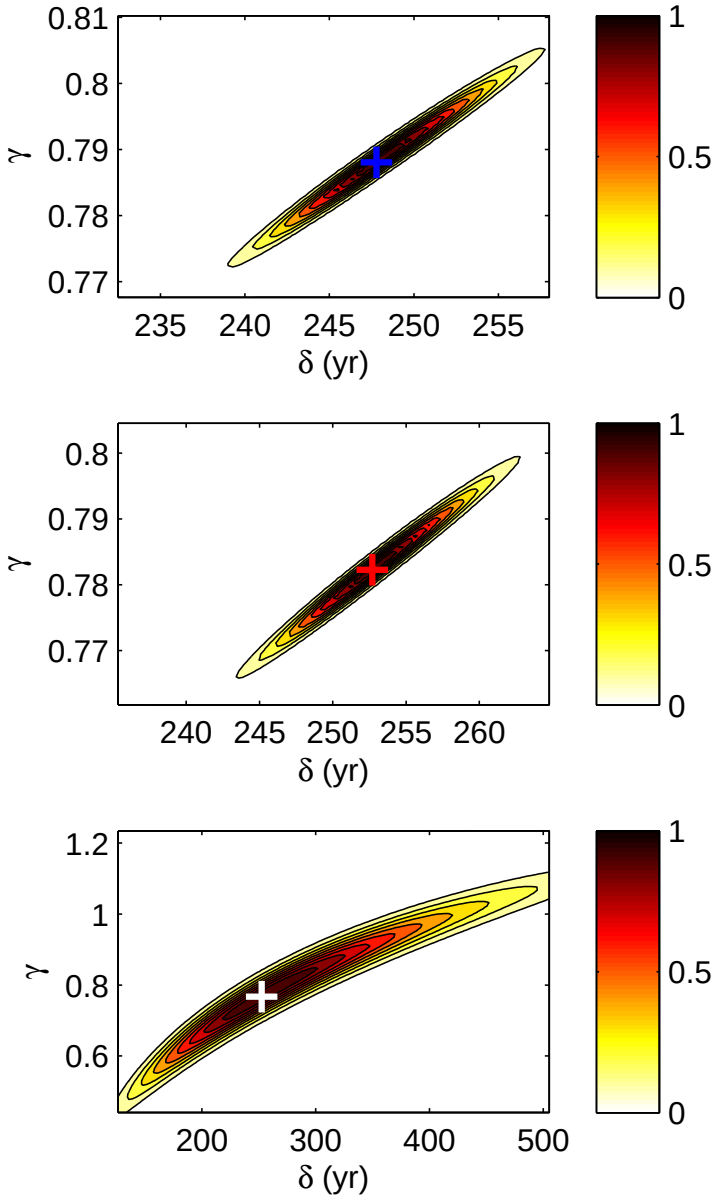

Figure A2. Probability density functions (normalized by their maximum value) for values of δ and γ (see equation 16) for the S0 simulation deduced from averaged τ_n^* estimated using Gauss coefficients after subtracting their averaged value (top), from $\bar{\tau}_n$ using original Gauss coefficients (middle), and from an instantaneous $\hat{\tau}_n$ (bottom). Crosses indicate the maximum likelihood parameters.

decreasing with n ($\beta \simeq 0.9$) for S1. The values of γ for our simulations range from 0.75 to 1.3 (from average spectra), encompassing the value $\gamma = 1$ favored by Lhuillier et al. (2011b) and found for the CE simulation. The most extreme (lowest viscosity, strongest forcing) simulation S1 shows the steepest decrease of τ_n with n (larger value of γ). S1 thus gives the closest value of γ to the instantaneous estimate from geomagnetic observations. For CE and S1, γ is decreased by about 5% when removing the time-average Gauss coefficients in the estimations of R_n and τ_n. Despite its relatively

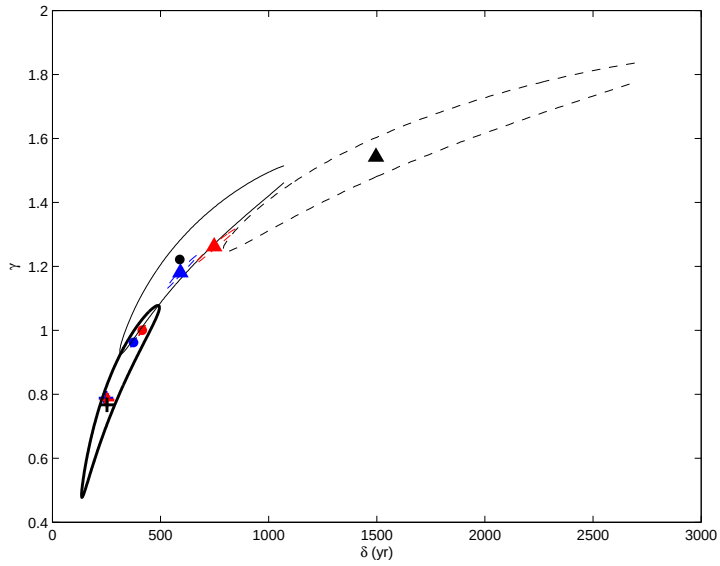

Figure A3. Curves of constant probability density (corresponding to 20% of the maximum probability) and maximum probability in the plane (δ, γ) obtained with the maximum likelihood method for one snapshot of each simulation S0 (black thick line and cross), CE (black thin line and filled circle), and S1 (black dashed line and triangle). For comparison, we also show the maximum probabilities from time-averages obtained while keeping (red) or not (blue) the average. Note that the probability functions obtained from time-averages are also represented but are restricted to too small parameter space to be visible on this figure.

modest forcing and viscosity and its specific torque and heat flux conditions, the simulation CE nevertheless presents a correlation time τ_n more sensitive to n than S0. Estimated values for δ encompass $\tau_{SV} = 415$ years (τ_{SV} is defined as δ for $\gamma = 1$). This time differs from τ_{SV} in the simulations S0 and S1, for which γ deviates significantly from 1, and it is close to τ_{SV} in the simulation CE for which $\gamma \simeq 1$.

If in average, parameters obtained from snapshot estimates $\hat{R}_n$ and $\hat{\tau}_n$ are mostly similar to those obtained using time-averaged, a r.m.s. mismatch of about 20% (resp. 5%) may be found between instantaneous and time-integrated estimates of the parameter γ (resp. β) defining the dependence of τ_n (resp. R_n) with the degree n. From Table A2, the two-sigma intervals found for γ in simulations S0, CE and S1 are respectively $[0.45, 1.05]$, $[0.70, 1.3]$, and $[0.85, 1.7]$ using the maximum likelihood method of Appendix A. Similar ranges of values are obtained by computing the probability density function obtained from a single snapshot of τ_n , as illustrated in Fig. A3.

		α		β	
		LSQ	ML	LSQ	ML
	(a)	147.0 ± 107.5	156.1 ± 86.3	1.05 ± 0.07	1.03 ± 0.05
S0	(b)	152.6	156.5	1.02	1.02
	(c)	143.1	148.4	1.02	1.01
	(a)	10.2 ± 5.9	11.0 ± 5.3	1.00 ± 0.05	0.99 ± 0.04
CE	(b)	10.3	11.2	0.99	0.99
	(c)	8.6	9.7	1.01	1.00
	(a)	33.2 ± 16.6	42.5 ± 20.1	0.93 ± 0.04	0.91 ± 0.03
S1	(b)	37.5	37.7	0.91	0.91
	(c)	27.7	27.3	0.93	0.93

Table A1. Parameters (α, β) for simulations S0, CE and S1, estimated from the least-squares (LSQ) and maximum likelihood (ML) approaches. α is expressed in 10^9 nT^2 and β is dimensionless. (a) estimated from snapshot values $\hat{R}_n$ (average value $\pm$ standard deviation, for 10 independent epochs); and from the expected variances as in equation (15), either removing (c) or keeping (b) the average value of the coefficients.

		δ		γ	
		LSQ	ML	LSQ	ML
	(a)	$313 \pm 154(0.75 \pm 0.37)$	$278 \pm 128(0.67 \pm 0.31)$	0.81±0.18	0.75±0.15
S0	(b)	294(0.71)	253(0.61)	0.86	0.78
	(c)	284(0.68)	248(0.60)	0.85	0.79
	(a)	$500 \pm 153(1.20 \pm 0.37)$	$460 \pm 135(1.11 \pm 0.33)$	1.07±0.16	1.02±0.16
CE	(b)	461(0.97)	415(1.00)	1.05	1.00
	(c)	401(0.97)	375(0.90)	0.99	0.96
	(a)	$835 \pm 426(2.01 \pm 1.03)$	$939 \pm 409(2.26 \pm 0.99)$	1.22±0.27	1.29±0.22
S1	(b)	704(1.70)	748(1.80)	1.23	1.26
	(c)	585(1.41)	592(1.43)	1.17	1.18

Table A2. Parameters (δ, γ) for simulations S0, CE and S1, estimated from the least-squares (LSQ) and maximum likelihood (ML) approaches. δ is expressed in years (and in terms of τ_{SV} in parentheses) and γ is dimensionless. (a) estimated from snapshot values $\hat{\tau}_n$ (average value $\pm$ standard deviation, for 10 independent epochs); and from the expected variances as in equation (15), either removing (c) or keeping (b) the average value of the coefficients.